Magnetic Resonance Imaging 60 (2019) 85–92

Contents lists available at ScienceDirect

Magnetic Resonance Imaging

journal homepage: www.elsevier.com/locate/mri

Case report

# Quantitative analysis of spatial averaging effect on chemical shift imaging SNR and noise coherence with k-space sampling schemes

Byeong-Yeul Lee*, Xiao-Hong Zhu, Wei Chen*

*Center for Magnetic Resonance Research, Department of Radiology, University of Minnesota Medical School, MN, USA*

ARTICLE INFO

*Keywords:*
Chemical shift imaging
k-space sampling
Noise coherence
Point-spread function
Signal-to-noise ratio (SNR)
Spatial averaging

ABSTRACT

Spatial averaging of multiple voxels from high-resolution chemical shift imaging (hrCSI) is a common strategy for *in vivo* metabolic studies to achieve a better signal-to-noise ratio (SNR) for a region-of-interest. However, the mechanism about how the spatial averaging approach influences the respective spectral signal and noise and its relevance to the k-space sampling schemes remains unclear. Using three-dimension $^{17}O$ CSI technique with the weighted k-space sampling method of Fourier series window, we performed quantitative SNR comparisons between a single low-resolution CSI (lrCSI) voxel (being 27 times larger than the hrCSI voxel size) and the spatially averaged hrCSI voxels with matched sampling volume and location. We demonstrated that the averaged hrCSI voxel spectrum had a large SNR loss (> 4 times) compared to the lrCSI voxel, which was resulted from unmatched increases in signal (~1.9 fold) and noise (~9.3 fold). The signal increase was caused by the spatial overlapping between the adjacent hrCSI voxels. The substantial noise increase was mainly attributed to the strong noise coherence among hrCSI voxels acquired with the weighted k-space sampling. This study presents a quantitative relation between the k-space sampling schemes to an apparent SNR penalty of the spatial averaging approach. The information could be useful for designing CSI acquisition method and determination of optimal spatial resolution for *in vivo* metabolic imaging studies.

## 1. Introduction

*In vivo* chemical shift imaging (CSI) or MRS imaging (MRSI) provides a unique imaging tool for mapping cerebral metabolites and metabolic rates, and studying neurochemistry and neuroenergetics [1–7]. In particular, with increasing recognition of complex neurological disorders/disease, CSI has been clinically useful for the improved diagnosis in the infected tissue and longitudinal monitoring of the disease progress [8], and for advancing the understanding of pathophysiological mechanisms underlying diseases [9–12].

Due to low concentration of detectable brain metabolites in a range of few mM, signal-to-noise ratio (SNR) of CSI is a key consideration for *in vivo* metabolite quantification that is essential for reliable neurochemical profiling in the human brain [13–16]. A low-resolution CSI (lrCSI) provides a relatively high SNR, but the coarse voxel size leads to an increased partial volume effect (PVE). In contrast, a high-resolution CSI (hrCSI) approach is more prevalent in the basic and clinical research because of its better specificity for the identification of altered metabolism in the impaired tissue due to less PVE [17–21]. However, the lower SNR and a long scan time are a major drawback for quantitative assessment of metabolite concentrations and clinical applications, in particular, for low gyromagnetic ratio ($\gamma$) X-nuclear CSI (*e.g.*, $^{13}C$, $^{2}H$, $^{17}O$, and $^{31}P$). To overcome this limitation faced by most CSI applications, spatial averaging of multiple voxels from a hrCSI dataset is a common strategy to achieve an adequate SNR in a desired region of interest (ROI).

Given the relation between spatial resolution and SNR [22–24], it is assumed that SNR is linearly proportional to a voxel size [25]. However, this linear assumption becomes invalid in the presence of a strong static magnetic field ($B_0$) inhomogeneity or radiofrequency magnetic field ($B_1$) inhomogeneity in space or the point spread function (PSF) of a CSI voxel. For instance, compared to a lrCSI voxel, a hrCSI voxel had a smaller SNR penalty than the theoretical estimation owing to the improved $B_0$ inhomogeneity [26], resulting in an increase in the apparent relaxation time ($T_2^*$) [13].

Despite previous studies in the literature for addressing the relation between SNR and spatial resolution, the mechanism about how the spatial averaging of hrCSI voxels quantitatively influences the respective spectral signal and noise, thus, SNR remains unclear. In particular, the specific relevance of the k-space sampling scheme to SNR was not rigorously studied before.

In this work, we aimed to: i) perform quantitative signal, noise and

* Corresponding authors at: Center for Magnetic Resonance Research, University of Minnesota, 2021 Sixth Street SE, Minneapolis, MN 55455, USA.
*E-mail addresses:* bylee@umn.edu (B.-Y. Lee), wei@cmrr.umn.edu (W. Chen).

https://doi.org/10.1016/j.mri.2019.03.023
Received 12 October 2018; Received in revised form 25 March 2019; Accepted 27 March 2019

SNR comparisons between the spatially averaged hrCSI voxel and the lrCSI voxel with matched sampling volume and location; ii) study how the spatial averaging contributes to the signal change by calculating the voxel-overlapping ratio of the hrCSI voxels (*i.e.*, PSF); iii) study how the k-space sampling schemes contribute to the noise level of the summed hrCSI voxel by examining the inter-voxel noise coherence; and iv) develop a noise model to estimate the contribution of the measured noise correlation to the real summed noise level of the hrCSI voxels. To avoid the aforementioned confounding effect of $B_0$ inhomogeneity on the CSI SNR, we employed the low-γ X-nuclear $^{17}O$ CSI in which resonance linewidth is insensitive to $B_0$ inhomogeneity owing to the strong quadrupole moment relaxation, resulting in short $T_2^*$ and longitudinal relaxation time ($T_1$).

## 2. Methods

All magnetic resonance imaging experiments were carried out on a Siemens whole-body/90-cm bore 7 T human scanner (MAGNETOM, Erlangen, Germany). A multinuclear surface-coil probe consisting of a quadrature $^1H$ coil (297.2 MHz) for anatomic imaging and shimming, and a single-loop and passively decoupled $^{17}O$ coil (40.1 MHz, 5 cm diameter) for collecting $^{17}O$ CSI data from the human occipital lobe or a water phantom was used in this study.

All *in vivo* experiments were performed under the FDA specific absorption rate (SAR) limitation. Three healthy volunteers (mean age (SD) = 25.0 (4.6) years) participated in this study that was approved by the Institutional Review Board committee of the University of Minnesota. The written consent form was obtained from all subjects.

Anatomical $T_1$-weighted images were acquired using a magnetization prepared rapid gradient echo sequence (acquisition parameters: repetition time (TR) = 2400 ms, echo time (TE) = 2.4 ms, inversion recovery (TI) = 1500 ms, RF pulse flip angle (FA) = 7°, and 1 mm isotropic resolution) for guiding the selection of CSI slices and voxels.

### 2.1. 3D FSW CSI

The three-dimensional (3D) $^{17}O$ CSI method was used for this comparison study. To explore the relation between k-space sampling scheme and SNR of the averaged hrCSI voxels, we employed the Fourier Series Window (FSW) method, one of the common CSI techniques, allowing for precise spatial localization and fast acquisition. The FSW CSI technique has been described in detail in the literature [27–29]. Briefly, as shown in Fig. 1A, CSI data were acquired with the predetermined weighed k-space sampling pattern. Subsequently, the FSW window function with the desired Fourier coefficients was applied to the signals to achieve an optimal filter for a desired voxel shape for CSI application. For convenience, the spatial coordinate of voxel described by the window function ($W$) in one spatial domain $\theta(r)$ is defined with a phase angle ($\theta(r)$) between 0 and 2π, then

$$W(\theta(r) - \theta_q) = \sum_{n=0}^{N-1} w_n^q \exp\{in\theta(r)\}$$

where $w_n$ is the Fourier window coefficient, N is the number of phase encoding, and $W(\theta - \theta_q)$ is the window function. The voxel spectrum can be described by

$$S_w^q(\theta(r) - \theta_q) = \sum_{n=0}^{N-1} s_n(t) w_n^q \exp\{in\theta(r)\}$$

where $s_n(t)$ is the NMR signal in the time domain acquired in the $n^{th}$ phase-encoding step.

Based on the 3D FSW CSI method as employed in this work, weighted partial k-space data (57%) were acquired on the coronal plane and a cylindrical voxel shape was designed (Fig. 1B).

### 2.2. 3D CSI experiment

*In vivo* 3D $^{17}O$ FSW-CSI data were obtained from the human occipital lobe under full relaxation condition: TR = 100 ms ($^{17}O$ water $T_1$ relaxation time ~ 5–7 ms [30]), 3D phase encoding step = 9 × 9 × 7, nominal FA = 90°, number of signal average = 5 (total k-space data = 1610), number of FID complex points = 300, length of RF hard pulse = 500 μs, spectral bandwidth = 30 kHz, and total acquisition time = 2 min 41 s. Spectral receiver bandwidth of 30 kHz was applied to collect $^{17}O$ signals from the short $^{17}O$ $T_2$ and $T_2^*$ of water (few ms) for acquiring adequate FID complex data points [30]. For the SNR comparison, two different fields of view (FOVs) of 80 × 80 × 60 $mm^3$ and 240 × 240 × 180 $mm^3$ were employed for collecting the hrCSI and lrCSI data; that is, reducing the spatial resolution by a factor of 3 in a 3D hrCSI imaging in each dimension provides a volume decrease by a factor of 27, such that the 27 hrCSI voxels were summed to match the size of the lrCSI voxel (see Fig. 2).

For the phantom study, 3D $^{17}O$ FSW-CSI data were acquired using a spherical bottle of water solution (0.037% $H_2{}^{17}O$ natural abundance) at pH of 7.0. Two FOVs of 110 × 110 × 90 $mm^3$ and 330 × 330 × 270 $mm^3$ were employed for collecting the hrCSI and lrCSI data, respectively. The $^{17}O$ CSI data were acquired under full relaxation condition with the following parameters: TR = 500 ms, 3D phase encoding step = 9 × 9 × 7, nominal FA = 90°, number of signal average = 3 (total k-space data = 966), number of FID complex

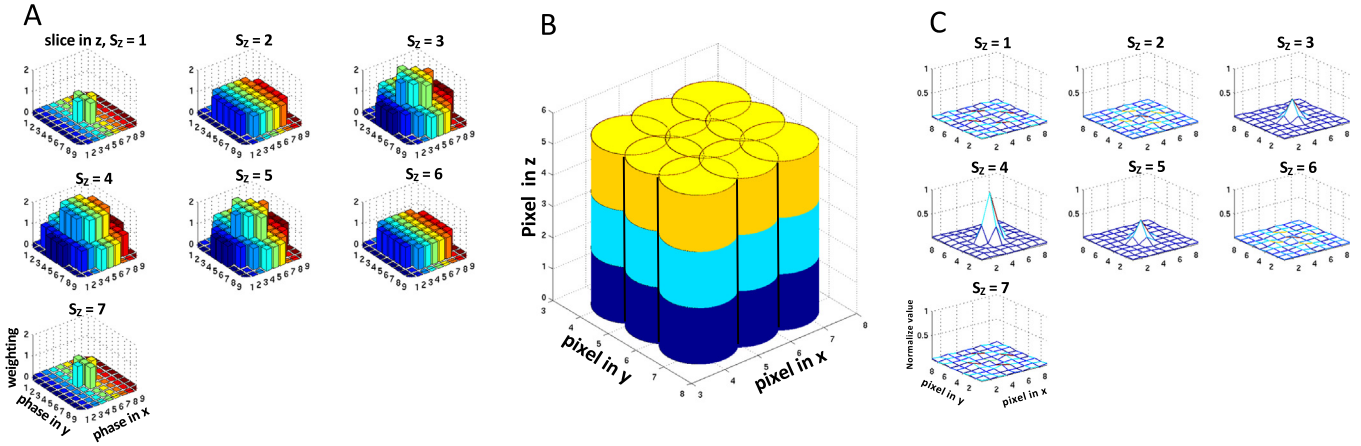


**Fig. 1.** The k-space sampling acquisition pattern and PSF of the FSW. (A) 2D projection of the k-space sampling pattern of the 3D FSW CSI method, showing a relatively high number of acquisition around the center of k-space. (B) The voxel geometry of 27 cylindrical voxels across three CSI slices. (C) PSF of the 3D FSW projected in the 2D image space. Abbreviation; FSW, Fourier series window; PSF, point-spread function.

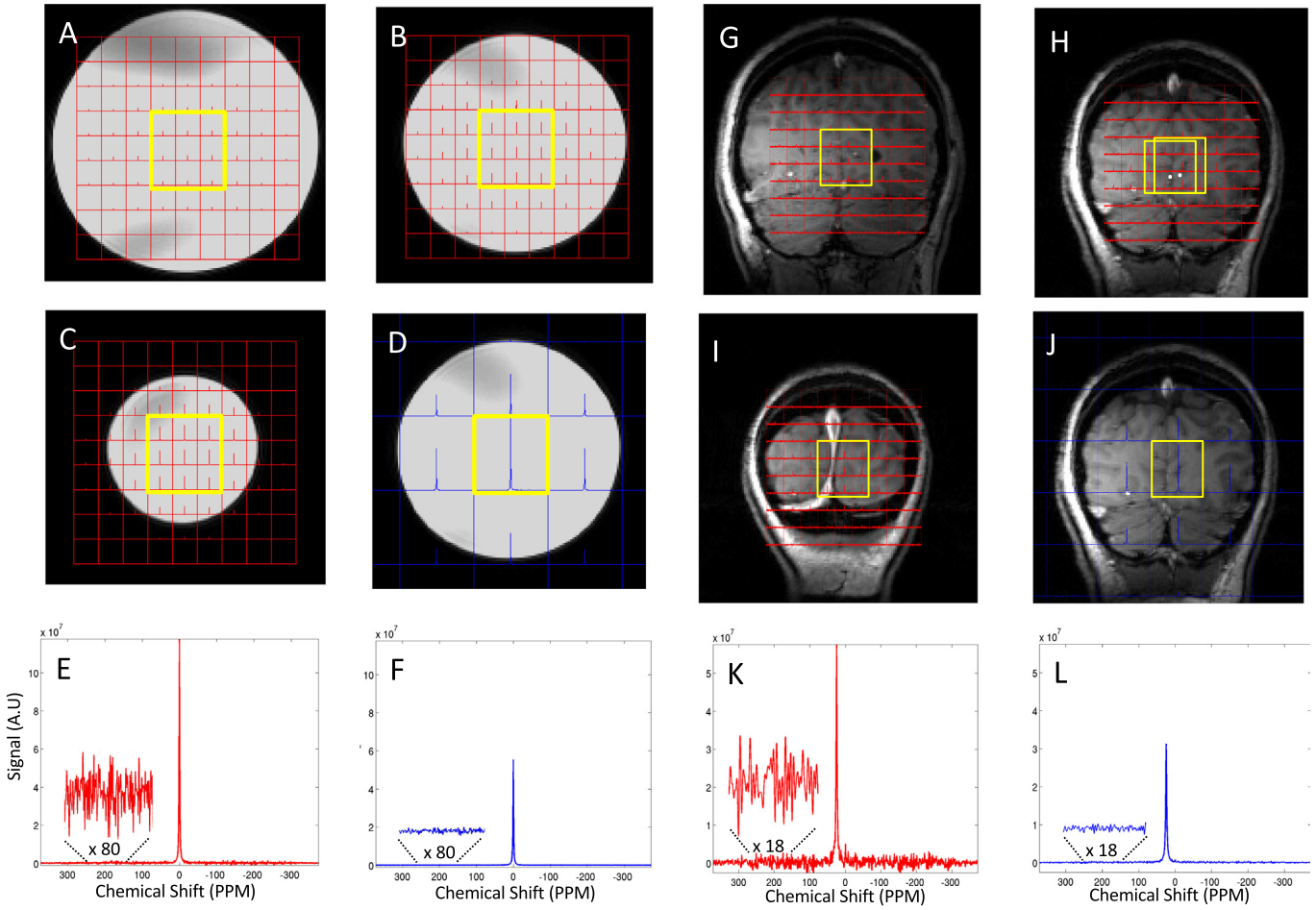


**Fig. 2.** Representative 3D $^{17}$O CSI slices of the natural abundant water signal in phantom and the human brain in the coronal orientation: (A-C) and (G-I) correspond to the three slices of high-resolution CSI (hrCSI) for the phantom and *in vivo* human brain, respectively; (D) and (J) represent a low-resolution CSI (lrCSI) slice of the phantom and *in vivo*, respectively. (E) and (F) represent the summed spectrum of 27 hrCSI voxels and a single voxel of lrCSI for the phantom, (K) and (L) correspond to a spectrum of the summed lrCSI voxels and a single lrCSI voxel for *in vivo* brain, respectively. The highlighted yellow boxes show the selection of 27 voxels in the hrCSI and the single voxel of the lrCSI with the same effective voxel size and location. The noise level of the phantom and *in vivo* brain were magnified by a factor of 80 (E and F) and 18 (K and L), respectively. (For interpretation of the references to colour in this figure legend, the reader is referred to the web version of this article.)

points = 512, length of RF hard pulse = 500 μs, and total acquisition time = 8 min and 3 s.

### 2.3. SNR analysis

For the SNR comparison, all $^{17}$O CSI FIDs were processed with zero-filling of 2048 data points. In order to match volume and location of the central lrCSI voxel, 27 hrCSI FIDs were selected from three middle slices of the hrCSI dataset (9 FIDs per slice) and were summed in the time domain prior to Fourier transform (see Fig. 2).

All SNR analyses were performed in the frequency domain. Signal was defined as the maximum amplitude of $H_2{}^{17}O$ spectral peak after phase correction. Noise was calculated using the standard deviation (SD) of the $^{17}$O spectra taken from a signal-free spectral baseline. Mean SD was computed by averaging SD from the left (0.1–0.3) and right side (0.7–0.9) of full spectral width range (0–1) to account for possible different noise levels between the two sides. All noise levels from the single ($\sigma$) and the summed voxel were compared. In addition, the summed noise level was compared to the theoretically estimated value ($\sigma\sqrt{N}$, N is the total number of voxels to be summed).

### 2.4. Modeling for noise correlation

To establish quantitative analysis between noise coherence and its contribution to real noise level of the averaged hrCSI voxel, we first computed noise correlation coefficient (NCC) from each of pair in the hrCSI voxels and the corresponding summed noise (*i.e.* SD). Using the NCC and SD values, the quantitative relation between these two parameters was derived using the linear regression:

$$SD = \alpha \times NCC + \beta \quad (1)$$

where $\alpha$ is a slope (*i.e.* regression coefficient) and $\beta$ is a y-intercept, which are determined by a regression fitting.

Using the established noise model in Eq. (1), the summed noise of the spatial averaging in CSI voxels ($\overline{SD}$) can be estimated as the following equations.

$$\begin{aligned} \overline{SD} &\cong (\alpha \times \overline{NCC} + \beta) \times \sqrt{N} \times \bar{\sigma}_N, \ N > 2 \\ \overline{SD} &\cong (\alpha \times \overline{NCC} + \beta) \times \bar{\sigma}_N, \ N = 2 \\ \overline{SD} &\cong \sigma, \ N = 1 \end{aligned} \quad (2)$$

where $\overline{NCC}$ is the mean noise correlation coefficient, $\bar{\sigma}_N$ is a mean SD of the single voxels ($=(\sum_{i=1}^{N} SD_i)/N$), N is the total number of voxels to be summed. The N number of highest NCC values was only included to calculate $\overline{NCC}$ ($=(\sum_{i=1}^{N} NCC_i)/N$) due to the weighted contribution to

the summed noise level.

For the validation of the noise model, the random noise, which is close to the pure random noise, was also generated using Matlab program (The Mathworks, Inc.) and the corresponding noise values ($\beta$) at NCC = 0 was compared to the theoretical estimation ($\sqrt{2}$).

### 2.5. $B_0$ analysis

To examine the differences in the $B_0$ field inhomogeneity of $^{17}O$ $H_2{}^{17}O$ signal between the two CSI resolutions (*i.e.*, linewidth variation), a spectral linewidth was measured with spectral phase correction using the full-width at half-maximum (FWHM) of the resonance peak without using linewidth broadening.

### 2.6. $B_1$ analysis

On the basis of the intrinsic $B_1$ field gradients in conjunction with the $^{17}O$ surface coil, we accounted for the effects of the spatial variations of the $B_1$ field across the sample on the SNR by estimating reference voltage of each CSI voxel for reaching a 90-degree FA ($V_{90°}$). The $B_1$ analyses for RF transmit field ($B_1{}^+$) and receive field ($B_1{}^-$) were performed using a series of CSI data acquired with different RF transmitter voltages using the following equations: [31,32].

$$S \propto \rho \bullet B_1^- \bullet \sin(FA) \tag{3}$$

$$FA = \gamma \bullet \tau \bullet B_1^+ \bullet V \tag{4}$$

where S is the measured $^{17}O$ signal of water resonance, ρ is the water density, $\tau$ is the RF pulse width, V is the RF transmitter pulse voltage. The $B_1{}^-$ value in a relative scale was determined by the maximum $^{17}O$ signal reaching a 90-degree FA ($S_{90°}$) and $B_1{}^+$ was determined by the corresponding reference voltage of $V_{90°}$ that is inversely proportional to $B_1{}^+$. All $B_1$ analyses were performed using a custom-built program in Matlab (The Mathworks, Inc.).

### 2.7. Point spread function

Based on the real voxel geometry (*i.e.*, cross-section size and length) determined by the FSW method, the contribution of point spread function (PSF) to the signal of the summed hrCSI voxels was estimated by computing the spatial overlapping ratio between hrCSI voxels (Fig. 1).

## 3. Results

### 3.1. SNR analysis

All results of SNR comparison for the phantom and *in vivo* human brains are summarized in Table 1. Overall, there was an apparent and large SNR loss in the summed hrCSI voxels in the phantom (a factor of 4.7) and *in vivo* human brain (a factor of 5.3) as compared to the central lrCSI voxel with matched sampling volume and location. Notably, such SNR reduction from the averaged hrCSI voxels was mainly attributed to a substantial increase in the noise level (9.2 and 9.5 folds for the phantom and *in vivo* brain studies, respectively).

### 3.2. Signal analysis

Fig. 2 shows typical 3D CSI profiles of the natural abundant $H_2{}^{17}O$ signal acquired with the FSW method and the identification of the ROI (highlighted yellow box) used for SNR comparison. Both hrCSI and lrCSI data were acquired with the same RF pulse voltages (*i.e.* 50 V and 55 V for the phantom (Fig. 2A–D) and *in vivo* study (Fig. 2G–J), respectively), showing an adequate SNR of the hrCSI voxels for the SNR comparison.

As shown in Fig. 2E and K, the summed signals of the 27 hrCSI voxels were significantly increased by a factor of 2.06 ± 0.10 and 1.77 ± 0.03 for the phantom and *in vivo* studies, respectively, as compared to those of the single lrCSI voxel with matched sampling volume and location (Fig. 2F and L).

### 3.3. Noise analysis

Fig. 2E–F and K–L represent the typical noise of the phantom and *in vivo* brain obtained from the signal-free spectral baseline. The single-voxel noise was not different between the hrCSI voxels and the lrCSI voxel for both phantom and *in vivo* brain (< 1%). However, the noises of the summed hrCSI voxels shown in Fig. 2E and K were substantially increased by a factor of 9.19 ± 0.48 and 9.50 ± 0.20 for the phantom and *in vivo* human brain, respectively, compared to those of the lrCSI voxel (Fig. 2F and L).

### 3.4. Noise correlation analysis

Fig. 3A–D show the inter-voxel NCC maps between the 27 hrCSI voxels for the simulated random noise, phantom noise acquired with the regular full k-space acquisition, phantom noise acquired with FSW k-space acquisition, *in vivo* brain noise acquired with the FSW k-space acquisition, respectively. Using linear regression, the noise models (SD) are described as a function of NCC;

For the phantom noise acquired with the regular full k-space acquisition (Fig. 3F),

$$SD = (0.695 \times NCC + 1.429) \times \sqrt{N} \times \bar{\sigma}_N,\ N > 2 \tag{5}$$

For the phantom noise acquired with the FSW k-space acquisition (Fig. 3G),

$$SD = (0.573 \times NCC + 1.480) \times \sqrt{N} \times \bar{\sigma}_N,\ N > 2 \tag{6}$$

For the noise of *in vivo* brain acquired with the FSW k-space acquisition (Fig. 3H),

$$SD = (0.539 \times NCC + 1.406) \times \sqrt{N} \times \bar{\sigma}_N,\ N > 2 \tag{7}$$

These models showed a statistically significant correlation (Pearson correlation, rho > 0.5, two-tailed $p < 0.0001$), confirming the linear relation between SD and NCC. For the further validation of the proposed noise modeling described in Eq. (2), we compared the summed theoretical noise values for the pure random noise with no noise coherence (NCC = 0). Based on the summed noise from pure random noise ($\sqrt{2}$ = 1.41, $N$ = 2, NCC = 0), the proposed noise models (Eqs. (5)–(7)) provided the similar noise values ($\beta$ in Eq. (2), at NCC = 0), confirming the reliable linear noise models: the simulated random noise (1.415, Fig. 3E), phantom with acquired with regular full k-space acquisition (1.429, Fig. 3F) and FSW k-space sampling (1.480, Fig. 3G), and *in vivo* noise model (1.406, Fig. 3H).

As expected, noise coherence was not observed in the random noise (Fig. 3A). Notably, the apparent strong noise correlation was clearly shown in the weighted k-space sampling schemes as compared to the regular full k-space acquisition. The summed noise of the phantom acquired with a regular full k-space acquisition had a low mean NCC value ($\overline{NCC}$ = 0.15 ± 0.01, calculated from the noise correlation map shown in Fig. 3B), resulting in a noise ratio by a factor of 7.97 (Fig. 3F). In contrast, the summed noise from the FSW-CSI method had a significantly high mean NCC value for the phantom ($\overline{NCC}$ = 0.54 ± 0.04, calculated from the noise correlation map shown in Fig. 3C) and *in vivo* brain ($\overline{NCC}$ = 0.60 ± 0.02, calculated from the noise correlation map shown in Fig. 3D), resulting in an increased noise ratio by a factor of 9.30 ± 0.13 (Table 1A) and 8.97 ± 0.05 (Table 1B), which were close to the real measured noise ratio (9.19 and 9.50 for phantom and *in vivo* brain, respectively).

**Table 1**
The SNR comparison between the summed high-resolution (ΣhrCSI) voxels and the low-resolution (lrCSI) for the phantom (A) and *in vivo* human brain (B). All values indicate hrCSI, lrCSI, and the ratios of the summed hrCSI values to the lrCSI values in accordance with each RF transmitter voltage. $\overline{NCC}$ represents mean of 27 highest correlation coefficients among the hrCSI voxels. * is the ratio of the summed noise estimated from the noise correlation coefficients to the lrCSI using Eqs. (6) and (7).

A

| RF pulse voltage | $B_0$, FWHM (Hz) | | | $B_1^+$ | | | Signal | | | Noise | | | SNR | *Noise | |
|---|---|---|---|---|---|---|---|---|---|---|---|---|---|---|---|
| | ΣhrCSI | lrCSI | Ratio | ΣhrCSI | lrCSI | Ratio | ΣhrCSI | lrCSI | Ratio | ΣhrCSI | lrCSI | Ratio | Ratio | $\overline{NCC}$ | Ratio |
| 50 | 87.2 | 92.2 | 0.95 | 1.12 | 1.02 | 1.10 | 1.18E+08 | 5.54E+07 | 2.13 | 3.82E+05 | 3.82E+04 | 10.0 | 0.21 | 0.59 | 9.44 |
| 67 | 88.5 | 91.6 | 0.97 | 1.30 | 1.16 | 1.11 | 1.02E+08 | 4.87E+07 | 2.09 | 3.62E+05 | 4.03E+04 | 8.99 | 0.23 | 0.53 | 9.26 |
| 83 | 84.2 | 87.1 | 0.97 | 1.90 | 1.58 | 1.20 | 6.96E+07 | 3.57E+07 | 1.95 | 3.63E+05 | 3.97E+04 | 9.14 | 0.21 | 0.51 | 9.20 |
| Mean | 86.6 | 90.3 | 0.96 | 1.44 | 1.26 | 1.14 | 9.65E+07 | 4.66E+07 | 2.06 | 3.76E+05 | 3.92E+04 | 9.19 | 0.21 | 0.54 | 9.30 |
| SD | 2.2 | 2.8 | 0.01 | 0.41 | 0.29 | 0.06 | 2.47E+07 | 1.00E+07 | 0.10 | 2.02E+04 | 2.65E+02 | 0.48 | 0.01 | 0.04 | 0.13 |

B

| RF pulse voltage | $B_0$, FWHM (Hz) | | | $B_1^+$ | | | Signal | | | Noise | | | SNR | *Noise | |
|---|---|---|---|---|---|---|---|---|---|---|---|---|---|---|---|
| | ΣhrCSI | lrCSI | Ratio | ΣhrCSI | lrCSI | Ratio | ΣhrCSI | lrCSI | Ratio | ΣhrCSI | lrCSI | Ratio | Ratio | $\overline{NCC}$ | Ratio |
| 55 | 122.3 | 129.1 | 0.95 | 1.16 | 1.15 | 1.01 | 3.75E+07 | 2.10E+07 | 1.79 | 6.93E+05 | 7.36E+04 | 9.42 | 0.19 | 0.61 | 9.00 |
| 73 | 124.3 | 126.1 | 0.98 | 1.13 | 1.07 | 1.06 | 4.20E+07 | 2.36E+07 | 1.78 | 6.83E+05 | 7.30E+04 | 9.35 | 0.19 | 0.58 | 8.92 |
| 92 | 125.9 | 124.9 | 1.01 | 1.12 | 1.12 | 1.00 | 4.32E+07 | 2.41E+07 | 1.79 | 6.72E+05 | 6.92E+04 | 9.72 | 0.18 | 0.60 | 8.99 |
| Mean | 124.2 | 126.7 | 0.98 | 1.28 | 1.24 | 1.02 | 3.72E+07 | 2.09E+07 | 1.77 | 6.83E+05 | 7.19E+04 | 9.50 | 0.19 | 0.60 | 8.97 |
| SD | 1.8 | 2.2 | 0.03 | 0.29 | 0.25 | 0.03 | 7.74E+06 | 4.08E+06 | 0.03 | 1.05E+04 | 2.40E+03 | 0.20 | 0.003 | 0.02 | 0.05 |

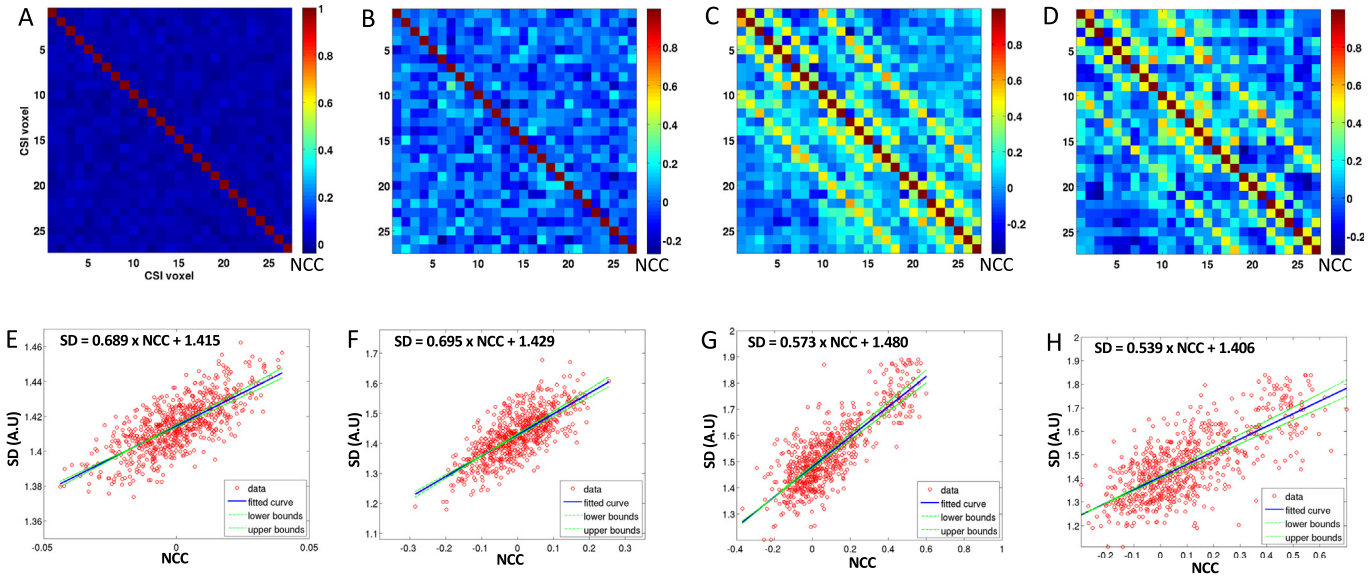


**Fig. 3.** Analysis of inter-voxel noise coherence of hrCSI voxels and a linear regression model. (A and E), (B and F), (C and G), and (D and H) represent the noise correlation matrix and corresponding linear regression for the simulated random noise, phantom noise with the full k-space acquisition, phantom noise with FSW, and *in vivo* brain noise with FSW, respectively. The colour bar represents the noise correlation coefficient. The linear regression model was displayed with a 95% confidence level (dotted green line) with a significant *P*-value < 0.05 using Pearson correlation analysis. Abbreviation; NCC, noise correlation coefficient; SD, standard deviation. (For interpretation of the references to colour in this figure legend, the reader is referred to the web version of this article.)

### 3.5. $B_0$ analysis

As expected from the insensitivity of $^{17}O$ CSI signal amplitude to $B_0$ inhomogeneity, the spectral linewidth between the two $^{17}O$ CSI resolutions was not significantly different (4% and 2% variation for the phantom and *in vivo* study, Table 1), ensuring the minimized confounding effects of $B_0$ inhomogeneity on the SNR results.

### 3.6. $B_1$ analysis

Fig. 4 displays a typical pattern of $B_1$ distribution for the single-loop $^{17}O$ surface coil, showing a large variation of the RF reference voltages reaching a $90^0$ flip angle ($V_{90}{}^o$) between the hrCSI voxels. There was no significant difference of contributions of $B_1$ inhomogeneity to the signal from two CSI resolutions, though, showing a slightly increased $B_1$ in the averaged hrCSI voxels (14% and 2% for the phantom and *in vivo*) relative to the lrCSI voxel (Table 1).

### 3.7. Point spread function

Based on the FSW k-space sampling pattern (Fig. 1A), voxel shape (Fig. 1B), and PSF (Fig. 1C), the spatial overlapping among the 27 hrCSI voxels was approximately 1.8 times as compared to a nominal voxel size, which was close to the ratio of signal increase of the summed 27

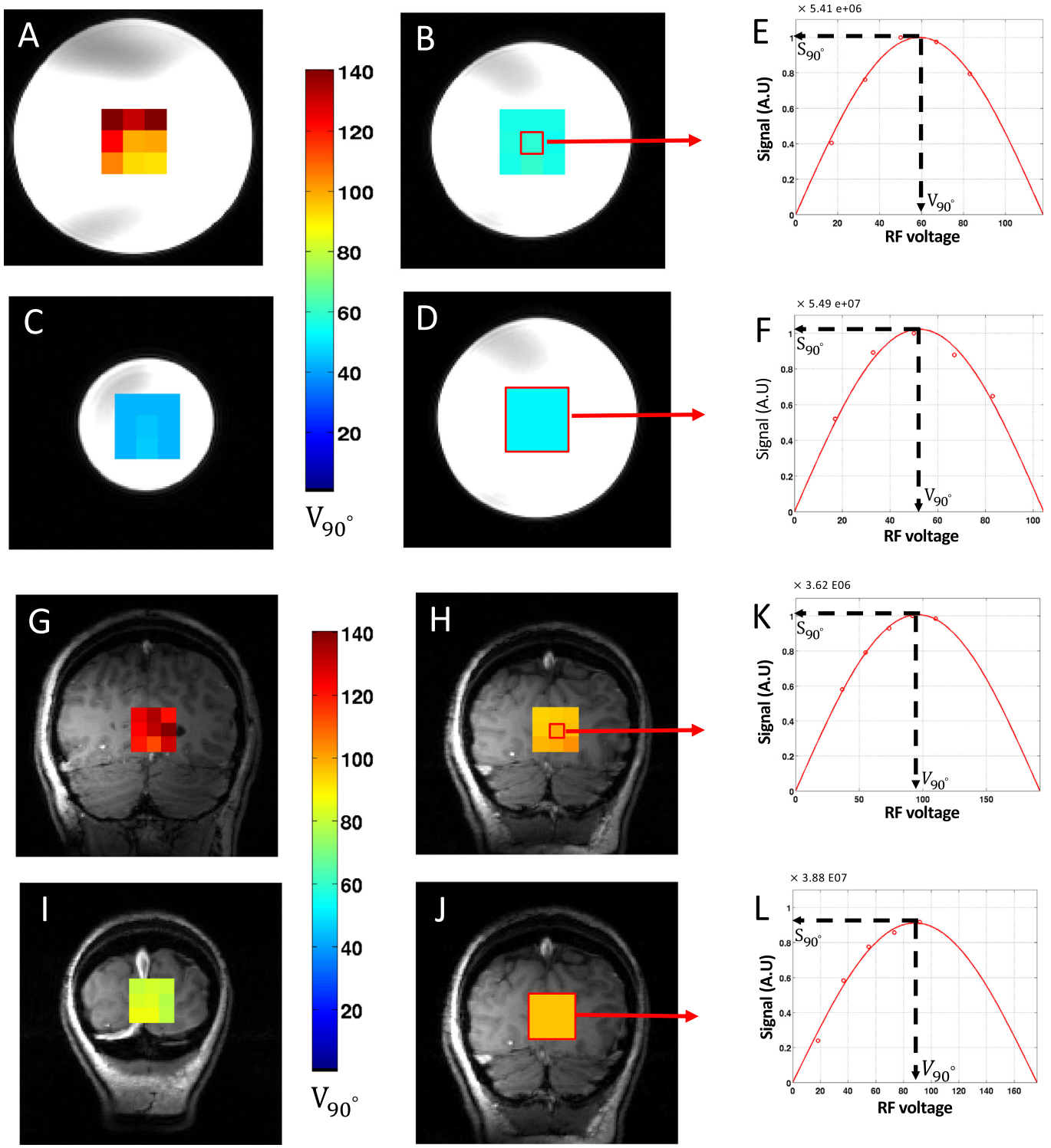


**Fig. 4.** Representative transmitter $B_1^+$ field maps for the phantom and the human brain in the coronal orientation. (A-C) and (G-I) correspond to the $B_1^+$ maps for the 27 voxels of the hrCSI for the phantom and *in vivo* human brain, respectively. (D) and (J) correspond to the $B_1^+$ values for the single voxel of the lrCSI for the phantom and *in vivo* human brain, respectively. (E and F) and (K and L) show $B_1^+$ analysis and regression for the voxels highlighted with a red box in (phantom, B and D) and (*in vivo*, H and J). Colour bars represent the reference voltages for achieving 90-degree flip angle ($V_{90^\circ}$) for each CSI voxel. (For interpretation of the references to colour in this figure legend, the reader is referred to the web version of this article.)

hrCSI voxels.

## 4. Discussion

In this study, we performed quantitative SNR analyses and comparisons for the spatial averaging of hrCSI voxels to examine the mechanism about how the voxel averaging approach contributes to the signal and noise level regarding the k-space sampling schemes. Major findings of the study are as follows: i) the spatial averaging of hrCSI voxels increased both signal and noise levels as compared to the lrCSI voxel with the same volume and location; ii) the signal increase was relevant to the point-spread function (or voxel-overlapping); iii), the

substantial noise increase of the summed voxels was mainly attributed to the inter-voxel noise coherence influenced by the PSF linked to the k-space sampling scheme, which was quantitatively estimated using the noise correlation models.

Theoretically, SNR of the averaged (or summed) voxels could be according to the $\sqrt{N}$ relation under the following key assumptions: the absence of $B_0$ and $B_1$ inhomogeneity, and random noise distribution in space, *i.e.*, independent voxel noise with a perfect PSF [25]. Although, spatial averaging of hrCSI voxels in this work reached the SNR loss (4.8 for phantom and 5.3 for *in vivo* study) close to the expected ratio of $\sqrt{N}$ (=5.2), however, the noise level of the summed voxel was significantly higher (9.19 and 9.50 for the phantom and *in vivo* human brain) than the theoretical estimation, indicating the assumption of random noise was not valid for the FSW CSI data due to a relatively large PSF.

From the PSF analysis in conjunction with a weighted k-space sampling scheme, we observed that the PSF contributed to the degree of signal and noise changes in the spatially averaged CSI data in a different manner. PSF affected the signal increase by a factor of the overlapping ratio measured between CSI voxels (or partial volume effect). On the other hand, PSF significantly increased the noise of the summed voxels by inducing phase coherence of noise spectra between the adjacent hrCSI voxels. Based on the estimation of the summed noise level with the proposed noise correlation models, SNR of the spatial averaging ($SNR_s$) of multiple hrCSI voxels could be described using the following equations:

$$\overline{S} = \left(\sum_{i=1}^{N} S_i\right) \propto \left(\sum_{i=1}^{N} \rho_i \bullet \sin(FA_i)\right) \bullet PSF$$

$$\overline{SD} = \alpha \times \overline{NCC} + \beta \bullet \sqrt{N} \bullet \overline{\sigma}_N$$

where $S_s$ is the summed signal, $S_i$ is the signal of each voxel, $\rho_i$ is the water spin density of each voxel, $FA_i$ is a flip angle of each voxel, N is a total number of the voxels, $SD(\overline{NCC})$ is a model for noise correlation, and $\overline{\sigma}_N$ is mean of the single-voxel noise level.

As one of the k-space sampling method with a window function, the FSW method used in the current study offers benefits for the accurate localization and the flexibility for determining voxel shape adjusted for the targeted regions. In fact, a number of the other fast CSI techniques have been proposed to overcome a major shortcoming of a long scan time [33]. Although these techniques also suffer from some of the limitations, based on the strong relationship between the degree of noise correlation and CSI sampling patterns in the present study, further investigation of this relationship with other fast CSI imaging techniques will provide useful information on the design of the CSI acquisition schemes in terms of SNR optimization.

As aforementioned, adequate spatial resolution is critical for *in vivo* metabolic imaging to achieve detection sensitivity as well as specificity [13–16]. Thereby, compared to the hrCSI approach, the apparent SNR loss observed from the hrCSI spatial averaging approach may have a negative impact on the reliable assessment of metabolite concentration. In particular, based on the presence of macromolecule in the human brain, the elevated noise level from summed hrCSI spectra could add more challenges for the precise baseline estimation, in particular for *in vivo* $^1$H MRS [34,35], requiring reliable fitting algorithms to avoid the overestimation of the metabolite concentrations. Thus, CSI approach with a proper spatial resolution optimized for covering the ROI (*e.g.*, brain tumor or stroke lesion) could be a better strategy for improving measurement sensitivity and reliability. Furthermore, in the case for the ROI containing a mixture of different tissue types, proper resolution of CSI voxels needs to be determined to avoid the PVE artifacts [13,36].

## 5. Conclusion

This study demonstrates the apparent SNR penalty of spatial averaging approach and the mechanism by which the k-space sampling schemes influences CSI SNR of the voxel averaging. Although this study focused on the FSW-based k-space scheme for the demonstration, the same analysis approach can be readily employed to other CSI or MRI k-space schemes. Therefore, the finding could be useful for the generic design of CSI acquisition method and determination of optimal spatial resolution for *in vivo* metabolic studies, in particular for human diseases.

## Acknowledgments

This work was supported by NIH Grants RO1 NS057560, NS070839 and MH111413, U01 EB026978, R24 MH106049, S10 RR026783, P41 EB015894, and P30 NS076408; and the W.M. Keck Foundation. The authors thank Hannes M. Wiesner for technical support and assistance.

## Disclosure

The authors declare no conflict of interest.

## References

[1] Ackerman JJ, Grove TH, Wong GG, Gadian DG, Radda GK. Mapping of metabolites in whole animals by $^{31}$P NMR using surface coils. Nature 1980;283(5743):167–70.
[2] Brown TR, Kincaid BM, Ugurbil K. NMR chemical shift imaging in three dimensions. Proc Natl Acad Sci U S A 1982;79(11):3523–6.
[3] Maudsley AA, Hilal SK, Perman WH, Simon HE. Spatially resolved high resolution spectroscopy by "four-dimensional" NMR. J. Magn. Reson. (1969) 1983;51(1):147–52.
[4] Zhu XH, Zhang N, Zhang Y, Zhang X, Ugurbil K, Chen W. In vivo $^{17}$O NMR approaches for brain study at high field. NMR Biomed 2005;18(2):83–103.
[5] Zhu XH, Lu M, Lee BY, Ugurbil K, Chen W. In vivo NAD assay reveals the intracellular NAD contents and redox state in healthy human brain and their age dependences. Proc Natl Acad Sci U S A 2015;112(9):2876–81.
[6] Lee BY, Zhu XH, Woo MK, Adriany G, Schillak S, Chen W. Interleaved $^{31}$P MRS imaging of human frontal and occipital lobes using dual RF coils in combination with single-channel transmitter-receiver and dynamic B0 shimming. NMR Biomed 2018;31(1).
[7] Coman D, Sanganahalli BG, Cheng D, McCarthy T, Rothman DL, Hyder F. Mapping phosphorylation rate of fluoro-deoxy-glucose in rat brain by $^{19}$F chemical shift imaging. Magn Reson Imaging 2014;32(4):305–13.
[8] Kizu O, Naruse S, Furuya S, Morishita H, Ide M, Maeda T, et al. Application of proton chemical shift imaging in monitoring of gamma knife radiosurgery on brain tumors. Magn Reson Imaging 1998;16(2):197–204.
[9] Thomas MA, Lipnick S, Velan SS, Liu X, Banakar S, Binesh N, et al. Investigation of breast cancer using two-dimensional MRS. NMR Biomed 2009;22(1):77–91.
[10] Klomp DW, Bitz AK, Heerschap A, Scheenen TW. Proton spectroscopic imaging of the human prostate at 7 T. NMR Biomed 2009;22(5):495–501.
[11] Banakar S, Thomas MA, Deveikis A, Watzl JQ, Hayes J, Keller MA. Two-dimensional $^1$H MR spectroscopy of the brain in human immunodeficiency virus (HIV)-infected children. J Magn Reson Imaging 2008;27(4):710–7.
[12] Sijens PE, Dorrius MD, Kappert P, Baron P, Pijnappel RM, Oudkerk M. Quantitative multivoxel proton chemical shift imaging of the breast. Magn Reson Imaging 2010;28(3):314–9.
[13] Gruber S, Mlynarik V, Moser E. High-resolution 3D proton spectroscopic imaging of the human brain at 3 T: SNR issues and application for anatomy-matched voxel sizes. Magn Reson Med 2003;49(2):299–306.
[14] Bartha R. Effect of signal-to-noise ratio and spectral linewidth on metabolite quantification at 4 T. NMR Biomed 2007;20(5):512–21.
[15] Macri MA, Garreffa G, Giove F, Guardati M, Ambrosini A, Colonnese C, et al. In vivo quantitative $^1$H MRS of cerebellum and evaluation of quantitation reproducibility by simulation of different levels of noise and spectral resolution. Magn Reson Imaging 2004;22(10):1385–93.
[16] Kreis R. Issues of spectral quality in clinical $^1$H-magnetic resonance spectroscopy and a gallery of artifacts. NMR Biomed 2004;17(6):361–81.
[17] Hu J, Feng W, Hua J, Jiang Q, Xuan Y, Li T, et al. A high spatial resolution in vivo $^1$H magnetic resonance spectroscopic imaging technique for the human breast at 3 T. Med Phys 2009;36(11):4870–7.
[18] Lam F, Liang ZP. A subspace approach to high-resolution spectroscopic imaging. Magn Reson Med 2014;71(4):1349–57.
[19] Mazumder A, Kumar A, Purohit AK, Dubey DK. A high-resolution phosphorus-31 nuclear magnetic resonance (NMR) spectroscopic method for the non-phosphorus markers of chemical warfare agents. Anal Bioanal Chem 2012;402(4):1643–52.
[20] Shim H, Wei L, Holder CA, Guo Y, Hu XP, Miller AH, et al. Use of high-resolution volumetric MR spectroscopic imaging in assessing treatment response of glioblastoma to an HDAC inhibitor. AJR Am J Roentgenol 2014;203(2):W158–65.
[21] van der Velden TA, Italiaander M, van der Kemp WJ, Raaijmakers AJ, Schmitz AM, Luijten PR, et al. Radiofrequency configuration to facilitate bilateral breast $^{31}$P MR spectroscopic imaging and high-resolution MRI at 7 tesla. Magn Reson Med 2015;74(6):1803–10.

[22] Kale SC, Lerch JP, Henkelman RM, Chen XJ. Optimization of the SNR-resolution tradeoff for registration of magnetic resonance images. Hum Brain Mapp 2008;29(10):1147–58.
[23] Kale SC, Chen XJ, Henkelman RM. Trading off SNR and resolution in MR images. NMR Biomed 2009;22(5):488–94.
[24] Noworolski SM, Nelson SJ, Henry RG, Day MR, Wald LL, Star-Lack J, et al. High spatial resolution $^{1}$H-MRSI and segmented MRI of cortical gray matter and subcortical white matter in three regions of the human brain. Magn Reson Med 1999;41(1):21–9.
[25] Edelstein WA, Glover GH, Hardy CJ, Redington RW. The intrinsic signal-to-noise ratio in NMR imaging. Magn Reson Med 1986;3(4):604–18.
[26] Li BS, Regal J, Gonen O. SNR versus resolution in 3D $^{1}$H MRS of the human brain at high magnetic fields. Magn Reson Med 2001;46(6):1049–53.
[27] Garwood M, Schleich T, Robin Bendall M, Pegg DT. Improved fourier series windows for localization in in vivo NMR spectroscopy. J. Magn. Reson. (1969) 1985;65(3):510–5.
[28] Garwood M, Schleich T, Ross BD, Matson GB, Winters WD. A modified rotating frame experiment based on a Fourier-series window function - application to Invivo spatially localized Nmr-spectroscopy. J Magn Reson 1985;65(2):239–51.
[29] Hendrich K, Hu X, Menon RS, Merkle H, Camarata P, Heros R, et al. Spectroscopic imaging of circular voxels with a two-dimensional Fourier-series window technique. J Magn Reson B 1994;105(3):225–32.
[30] Zhu XH, Merkle H, Kwag J, Ugurbil K, Chen W. $^{17}$O relaxation time and NMR sensitivity of cerebral water and their field dependence. Magn Reson Med 2001;45(4):543–9.
[31] Hoult DI. The principle of reciprocity in signal strength calculations—a mathematical guide. Concepts Magn. Reson. 2000;12(4):173–87.
[32] Lee BY, Zhu XH, Rupprecht S, Lanagan MT, Yang QX, Chen W. Large improvement of RF transmission efficiency and reception sensitivity for human in vivo $^{31}$P MRS imaging using ultrahigh dielectric constant materials at 7T. Magn Reson Imaging 2017;42:158–63.
[33] Pohmann R, von Kienlin M, Haase A. Theoretical evaluation and comparison of fast chemical shift imaging methods. J Magn Reson 1997;129(2):145–60.
[34] BK L, RD L, SD D, POA C. Analysis of macromolecule resonances in $^{1}$H NMR spectra of human brain. Magn Reson Med 1994;32(3):294–302.
[35] ME J, Bheeshma R, BK M, RG K. Phospholipid bilayer contribution to $^{31}$P NMR spectra in vivo. Magn Reson Med 1989;12(2):282–9.
[36] Hanson LG, Adalsteinsson E, Pfefferbaum A, Spielman DM. Optimal voxel size for measuring global gray and white matter proton metabolite concentrations using chemical shift imaging. Magn Reson Med 2000;44(1):10–8.